

High-Performance Pseudocapacitive Microsupercapacitors from Laser-Induced Graphene

Lei Li, Jibo Zhang, Zhiwei Peng, Yilun Li, Caitian Gao, Yongsung Ji, Ruquan Ye, Nam Dong Kim, Qifeng Zhong, Yang Yang, Huilong Fei, Gedeng Ruan, and James M. Tour*

The development and miniaturization of energy storage devices are facilitating the growth of modern microelectronic systems.^[1–3] Microbatteries are presently the major power source for miniaturized electronic devices even though they suffer from sluggish charge/discharge processes and a limited cycle life.^[2–7] Microsupercapacitors (MSCs), on the other hand, have high power density, fast charge/discharge rates, and long service life. And with their in-plane interdigitated electrodes, they show a pathway to replace microbatteries.^[2–7] However, developing easily fabricated MSCs with high energy densities, close to or exceeding those in microbatteries, without sacrificing other electrochemical characteristics, is a crucial challenge.^[4,8] The most common strategy is to use photolithography to prepare interdigitated patterns of highly conductive carbon materials to provide the electrochemical double layer capacitance (EDLC).^[8–14] Recently, laser writing technology has also been used to reduce and pattern graphene oxide (GO) as interdigitated electrodes in MSCs.^[15–17] However, the synthesis and postreaction treatment of GO and the problematic stability of the remaining GO in such devices present commercialization challenges.^[18,19] Since the energy density of the

device is determined by its capacitance and working voltage ($E = CV^2/2$),^[20] further improvement of its energy storage relies on enhancing either of these parameters. To increase device capacitance, pseudocapacitive materials, such as transition metal oxides^[10,12,21–23] and electrically conductive polymers,^[24,25] are loaded onto the electrodes to provide pseudocapacitance from surface redox reactions. However, this fabrication strategy is limited by either high-cost patterning processes or harsh synthetic conditions, slowing deployment in commodity electronic devices. Alternatively, organic electrolytes are used for their higher working voltage, resulting in further improvement in energy storage.^[26] However, safety issues, complex fabrication processes, and strict conditions for the use of organic electrolytes have limited their widespread application.^[26] An alternative approach is to make asymmetric MSCs without using an organic electrolyte.^[27]

Recently, our group developed a simple and scalable method to prepare patterned porous graphene on a polyimide (PI) substrate by laser-writing patterns in air, and the resulting laser-induced graphene (LIG) showed its promising applications in miniaturized energy storage devices.^[28–30] Here, we combine the laser induction process with subsequent electrodeposition of pseudocapacitive materials for the fabrication of all-solid-state, flexible symmetric and asymmetric MSC devices that show greatly improved electrochemical performance. A CO₂ laser is first used to convert the PI into porous LIG with an interdigitated architecture, which works not only as EDLC electrodes but also as a flexible and conductive matrix for the electrodeposition of pseudocapacitive materials. Two types of pseudocapacitive materials, manganese dioxide (MnO₂) or ferric oxyhydroxide (FeOOH), and polyaniline (PANI), representing characteristic transition metal oxides and conductive polymers, are electrodeposited onto the LIG forming LIG–MnO₂, LIG–FeOOH, and LIG–PANI composites. They are then assembled into all-solid-state flexible symmetric LIG–MnO₂–MSCs and LIG–PANI–MSCs, and asymmetric MSCs using LIG–FeOOH as a negative electrode and LIG–MnO₂ as a positive electrode (LIG–FeOOH//LIG–MnO₂) that are free of current collectors, binders, and separators due to the well-defined patterns that avoid short circuiting the electrodes. All of these devices demonstrate comparable energy densities to microbatteries without sacrificing their good rate performance, cycling stability, and mechanical flexibility.

The two-step syntheses of the hybrid materials, LIG–MnO₂, LIG–FeOOH, and LIG–PANI, and the fabrication into MSCs are shown in **Figure 1a**. CO₂ laser induction of the PI substrate was first conducted to form patterned LIG with 12 in-plane interdigitated electrodes (six per polarity), onto which

Dr. L. Li, J. Zhang, Dr. Z. Peng, Y. Li, C. Gao,
Dr. Y. Ji, R. Ye, Dr. N. D. Kim, Q. Zhong,
Dr. Y. Yang,^[†] Dr. H. Fei, Dr. G. Ruan, Prof. J. M. Tour
Department of Chemistry
Rice University
6100 Main Street, Houston, TX 77005, USA
E-mail: tour@rice.edu



C. Gao
School of Physical Science and Technology
Lanzhou University
Lanzhou 730000, China
Q. Zhong
State Key Laboratory of Bioelectronics
School of Biological Science and Medical Engineering
Southeast University
Nanjing 210096, China
Dr. Y. Yang, Prof. J. M. Tour
Smalley Institute for Nanoscale Science and Technology
Rice University
6100 Main Street, Houston, TX 77005, USA
Prof. J. M. Tour
Department of Material Science and NanoEngineering
Rice University
6100 Main Street, Houston, TX 77005, USA

^[†]Present address: NanoScience Technology Center, University of Central Florida, 12424 Research Parkway, Suite 400, Orlando, FL 32826, USA

DOI: 10.1002/adma.201503333

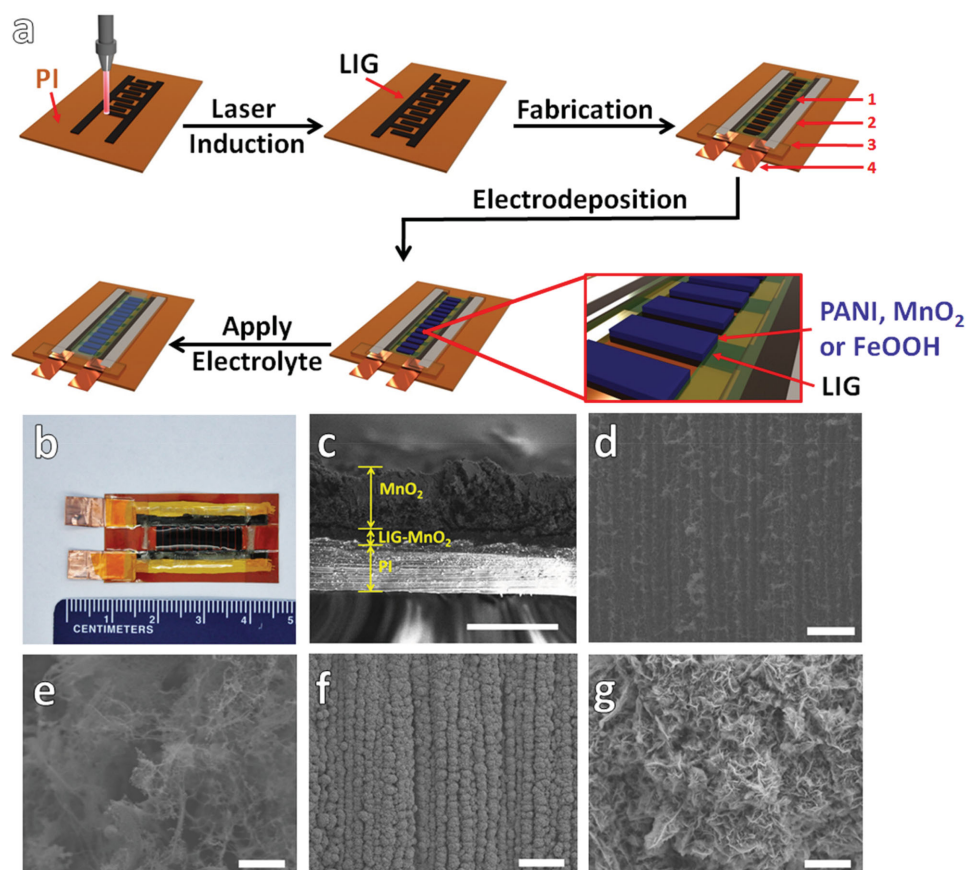


Figure 1. Fabrication and the structural morphology of the LIG-MnO₂-MSC. a) Scheme of the fabrication of MSCs with LIG-MnO₂, which is similar to the formation of LIG-FeOOH, or LIG-PANI. 1, 2, 3, and 4 are epoxy adhesive, silver paste, Kapton tape and copper tape, respectively. b) Digital photograph of one MSC device. c) Cross-sectional SEM images of LIG-MnO₂. Scale bar is 100 μm. SEM images of top view of d,e) LIG, and f,g) MnO₂ in LIG-MnO₂. Scale bars are 100 μm for Figure (d) and (f) and 2 μm for (e) and (g). The lined pattern in (d) and (f) is due to raster scanning of the laser.

the pseudocapacitive materials, MnO₂, FeOOH, or electrically conductive PANI, were electrodeposited to form the composites of LIG-MnO₂, LIG-FeOOH, or LIG-PANI. The amount of MnO₂, FeOOH, or PANI in the composites was easily controlled by adjusting the deposition time or cycles, and here labeled as LIG-MnO₂-X and LIG-FeOOH-X (where X represents the deposition time), and LIG-PANI-Y (where Y represents the number of deposition cycles). Details for LIG synthesis and electrodeposition of MnO₂, FeOOH, or PANI can be found in the Experimental Section. Solid-state polymer electrolyte containing poly(vinyl alcohol) (PVA) was used to complete the fabrication of the MSC devices. MSCs of various sizes can be prepared on demand by computer-controlled patterning in air at room temperature during the laser induction process (Figure S1, Supporting Information). Figure 1b shows a digital photograph of one fully fabricated MSC device using this method. Figure 1c shows the cross-sectional scanning electron microscopy (SEM) images of LIG-MnO₂-2.5 h, in which MnO₂ was observed to deposit into the LIG layer. The average thickness of the composite depends on the electrodeposition time or cycles and increases from 34 μm of LIG alone to 101 μm of LIG-MnO₂-4.0 h, 76 μm of LIG-PANI-15, and 41 μm of LIG-FeOOH-1.5 h (Figures S2–S5a, Supporting Information). Figure 1d–g shows the top view SEM images of

LIG and MnO₂, respectively. While LIG forms a porous thin film structure that could work as a conductive matrix for the subsequent electrodepositions, the deposited MnO₂ forms a flower-like shape. The cross-sectional and top view SEM images of LIG-FeOOH and LIG-PANI are also provided in Figure S5 (Supporting Information). The morphologies of LIG-MnO₂, LIG-FeOOH, and LIG-PANI are further characterized by transmission electron microscopy as shown in Figures S6–S8 (Supporting Information). Crystallized MnO₂, FeOOH, and nanofibril PANI were found to directly deposit onto the LIG. Raman spectroscopy, X-ray diffraction, and X-ray photoelectron spectroscopy were also used to study the composite compositions (Figure S9, Supporting Information).^[30–33]

We first studied the electrochemical performance of LIG-MnO₂-MSCs with LiCl/PVA as the electrolyte using cyclic voltammetry (CV) and galvanostatic charge–discharge experiments in a potential window from 0 to 1.0 V. Figure 2a shows the CV curves of LIG-MnO₂-X and LIG at a scan rate of 5 mV s^{−1}. Although LIG is known to contribute capacitance by the EDLC mechanism,^[28–30] the CV curve of LIG is minuscule compared to those of LIG-MnO₂-X, demonstrating that most of the capacitance comes from the pseudocapacitance of MnO₂. Also, aside from the much larger CV curve area, the pseudorectangular CV shape of LIG-MnO₂-X indicates good

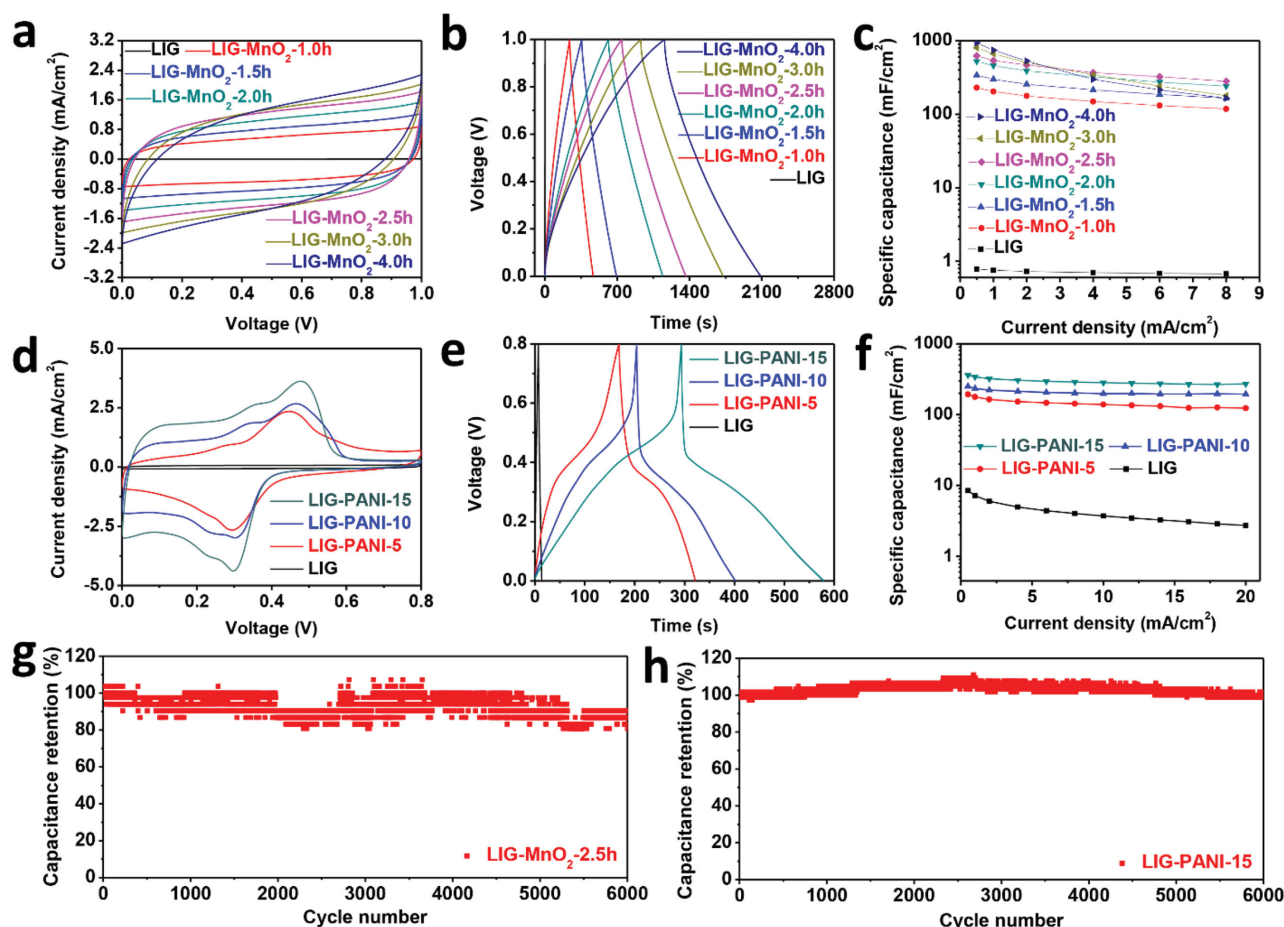


Figure 2. Electrochemical performance of LIG-MnO₂ and LIG-PANI MSCs. a) CV curves of LIG-MnO₂-X and LIG at a scan rate of 5 mV s⁻¹. b) Galvanostatic charge-discharge curves of LIG-MnO₂-X and LIG at a current density of 0.5 mA cm⁻². c) Areal specific capacitance of LIG-MnO₂-X and LIG over a current density range of 0.5 and 8.0 mA cm⁻². d) CV curves of LIG-PANI-Y and LIG at a scan rate of 10 mV s⁻¹. e) Galvanostatic charge-discharge curves of LIG-PANI-Y and LIG at a current density of 0.5 mA cm⁻². f) Areal specific capacitance of LIG-PANI-Y and LIG over a current density range of 0.5 and 20.0 mA cm⁻². g) Cycling stability of LIG-MnO₂-2.5 h at the current density of 1.0 mA cm⁻². h) Cycling stability of LIG-PANI-15 at the current density of 0.8 mA cm⁻².

capacitive behavior.^[7] Figure S10 (Supporting Information) shows CV curves of LIG-MnO₂-X at a scan rate ranging from 2 to 100 mV s⁻¹, demonstrating a proportional current increase with an increasing scan rate. The distorted CV shapes of the samples with more MnO₂ content at high scan rates may result from the decreased electrical conductivity.^[34] Figure 2b shows the galvanostatic charge-discharge curves of LIG-MnO₂-X at a current density of 0.5 mA cm⁻². The curve from LIG alone is nearly negligible, again demonstrating little contribution in capacitance from LIG in the composite of LIG-MnO₂, which is consistent with the CV analyses.^[7] Figure S11 (Supporting Information) further shows the galvanostatic charge-discharge curves of these samples at varying current densities. The nearly symmetrical charging and discharging curves and small voltage drops at initial discharge states indicate good capacitive behavior and high conductivity within the electrodes.^[23] Based on the galvanostatic charge-discharge curves, the areal and volumetric specific electrode capacitance of LIG-MnO₂-X are calculated and plotted in Figure 2c and Figure S12 (Supporting Information). Here, the total area of each MSC device (A_{Device})

includes the interdigitated electrodes and the spaces between them, and the volume is equal to A_{Device} multiplied by the height of the composite (Figure S13, Supporting Information). More MnO₂ content in the LIG-MnO₂ composite results in a higher capacitance at low current density, as evidenced by the highest areal and volumetric specific capacitances of 934 mF cm⁻² and 93.4 F cm⁻³, respectively, from LIG-MnO₂-4.0 h at a current density of 0.5 mA cm⁻². At the same current density, the areal and volumetric specific capacitance of LIG alone is less than 0.8 mF cm⁻² and 0.2 F cm⁻³, indicating that most of the capacitance is coming from the pseudocapacitance of MnO₂ in the LIG-MnO₂ composite. With increasing current density, the capacitance from the sample with less MnO₂ decreases more slowly. At a high current density of 8.0 mA cm⁻², the specific capacitance of LIG-MnO₂-2.5 h is maximized, with an areal value of 281 mF cm⁻² and a volumetric value of 31.5 F cm⁻³, most likely due to the relatively higher conductivity of the LIG-MnO₂ composite when less MnO₂ was deposited.

LIG-PANI-MSCs using H₂SO₄/PVA as the electrolyte were also studied from CV and galvanostatic charge-discharge

experiments in a potential window from 0 to 0.8 V (Figure 2d,e and Figures S14 and S15, Supporting Information). Figure 2f and Figure S16 (Supporting Information) show the calculated areal and volumetric specific electrode capacitance of LIG-PANI-Y. LIG-PANI-15 has the best performance among all the samples with an areal and volumetric specific capacitance of 361 mF cm^{-2} and 47.5 F cm^{-3} , respectively, at a current density of 0.5 mA cm^{-2} . In comparison, LIG itself is only 8.4 mF cm^{-2} and 1.8 F cm^{-3} at the same current density. When the current density increases to 20 mA cm^{-2} , the specific capacitance of LIG-PANI-15 still remains at 271 mF cm^{-2} and 35.6 F cm^{-3} with a high capacitance retention of 75%, indicating the good rate performance of LIG-PANI-15. The cyclability of the fabricated devices from LIG-MnO₂ and LIG-PANI were also tested. After 6000 cycles of charge-discharging test, the capacitance of LIG-MnO₂-2.5 h and LIG-PANI-15 remained over 82% and 97%, respectively, showing good stability of the devices based on these hybrid composites (Figure 2g,h).

To meet the specific energy and power needs for practical applications, multiple MSCs from LIG-MnO₂ or LIG-PANI can also be scaled up and assembled in either series or parallel configurations (Figure S17, Supporting Information). Compared with a single MSC, the discharge time of three MSCs connected in parallel increased to 3× that of a single MSC when operated at the same current density. When the three MSCs were connected in series, it exhibited a 3× higher voltage window with a similar discharge time at the same current density. An alternative way to increase the voltage output is to make the asymmetric MSCs.^[27] Here, asymmetric MSCs of LIG-FeOOH//LIG-MnO₂ were constructed using

LIG-FeOOH in the negative electrodes (Figures S18 and S19, Supporting Information) and LIG-MnO₂ in the positive electrodes (Figures S20–S22, Supporting Information) while PVA/LiCl was used as the solid-state electrolyte. Figure 3a shows the CV curves of LIG-FeOOH//LIG-MnO₂ at different scan rates in the potential window of 0 to 1.8 V. Its nearly rectangular CV shape is indicative of good capacitive behavior. This is further supported by the triangular galvanostatic charge-discharge curves in the same potential window as shown in Figure 3b. The working voltage increased from 1.0 V in the case of LIG-MnO₂ symmetric MSCs to 1.8 V in LIG-FeOOH//LIG-MnO₂ asymmetric MSCs. One of the asymmetric MSCs can power a light emitting diode (1.7 V, 30 mA) (Figure S23, Supporting Information). Capacitance of the asymmetric MSCs is calculated based on charge-discharge curves in Figure 3b and Figure S24 (Supporting Information). Areal and volumetric capacitances of LIG-FeOOH//LIG-MnO₂ (full device capacitance) are 21.9 mF cm^{-2} and 5.4 F cm^{-3} , respectively, at a current density of 0.25 mA cm^{-2} (Figure 3c). When the current density increases to 10 mA cm^{-2} , 64% capacitance retention is seen. MSCs of LIG-MnO₂-2.5 h, LIG-PANI-15, and LIG-FeOOH//LIG-MnO₂ also showed high galvanostatic capacitance as shown in Figure S25 (Supporting Information). The cycling life of LIG-FeOOH//LIG-MnO₂ is also evaluated by the extended galvanostatic charge-discharge cycles. As shown in Figure 3d, 84% capacitance is retained after 2000 cycles, demonstrating a promising cycling stability.

The flexibility of MSCs from LIG-MnO₂-2.5 h, LIG-PANI-15, and LIG-FeOOH//LIG-MnO₂ was also studied as shown in Figure 4. The digital image of one MSC device

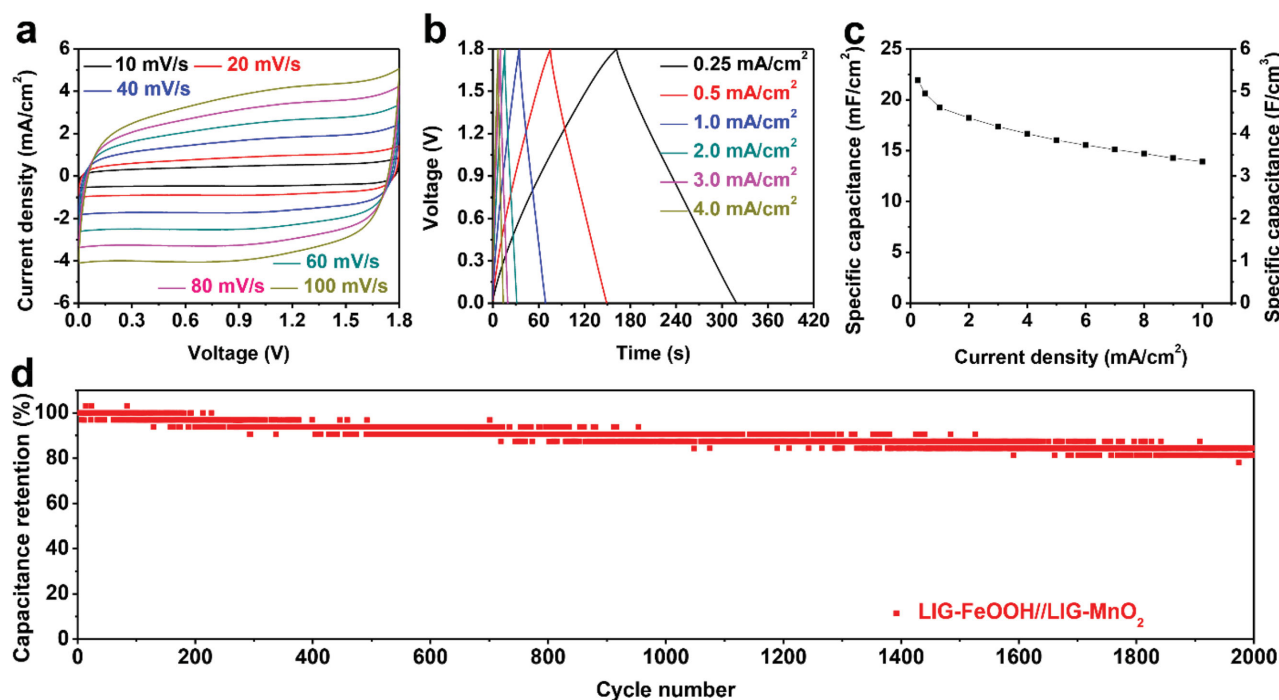


Figure 3. Electrochemical performance of LIG-FeOOH//LIG-MnO₂ asymmetric MSCs. a) CV curves of LIG-FeOOH//LIG-MnO₂ at a scan rate range of 10–100 mV s^{-1} . b) Galvanostatic charge-discharge curves of LIG-FeOOH//LIG-MnO₂ at a current density range of 0.25–4.0 mA cm^{-2} . c) Areal and volumetric specific capacitance of LIG-FeOOH//LIG-MnO₂ over a current density range of 0.25–10 mA cm^{-2} . d) Cycling stability of LIG-FeOOH//LIG-MnO₂ at the current density of 1.0 mA cm^{-2} .

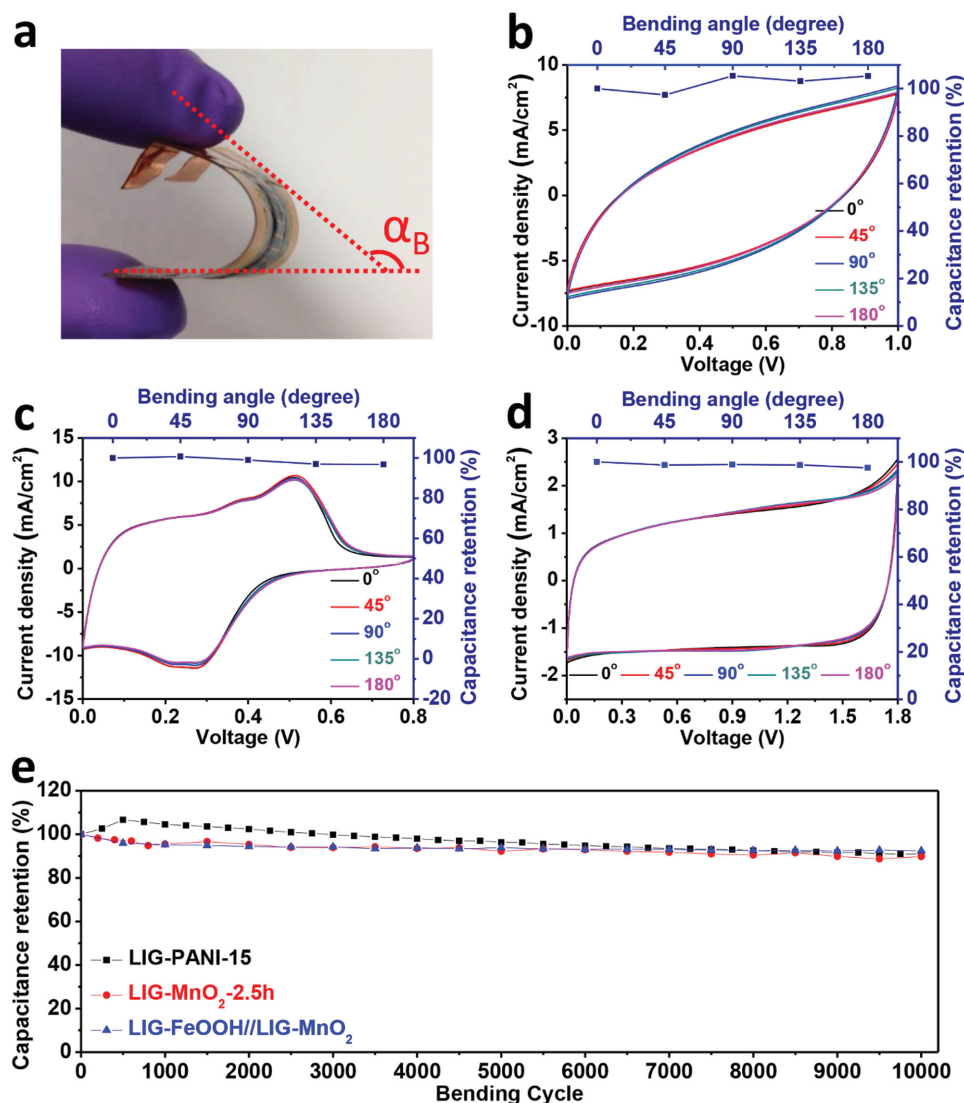


Figure 4. Flexibility testing of LIG-MnO₂-2.5 h, LIG-PANI-15, and LIG-FeOOH//LIG-MnO₂. a) Digital photograph of a device under bending. The angle labeled as α_B in the image is defined as the bending angle. CV curves and capacitance retention of b) LIG-MnO₂-2.5 h, c) LIG-PANI-15, and d) LIG-FeOOH//LIG-MnO₂ under bending angles of 0°, 45°, 90°, 135°, and 180° at a scan rate of 40 mV s⁻¹. e) Capacitance retention of LIG-MnO₂-2.5 h, LIG-PANI-15, and LIG-FeOOH//LIG-MnO₂ at different bending cycles with an α_B of $\approx 90^\circ$.

that is manually bent with a bending angle (α_B) of $\approx 135^\circ$ is shown in Figure 4a. The CV curves at different α_B are nearly overlapping with each other, and the calculated capacitance remains almost the same, indicating the stable performance of LIG-MnO₂, LIG-PANI, and LIG-FeOOH//LIG-MnO₂ at these states (Figure 4b–d). The flexibility tests carried out by bending the device with an α_B of $\approx 90^\circ$ (Figure 4e) show a good mechanical flexibility of these materials with only 10% capacitance decay after 10 000 bending cycles. The good mechanical flexibility is further demonstrated by the well-maintained morphologies of LIG-MnO₂-2.5 h after bending tests (Figure S26, Supporting Information) compared to the original one (Figure S3j–l, Supporting Information). Some small increase in performance at early cycles can be attributed to enhanced electrolyte penetration into the LIG-PANI-15. These results demonstrate that all three of the MSCs,

LIG-MnO₂-2.5 h, LIG-PANI-15, and LIG-FeOOH//LIG-MnO₂, are effective flexible MSCs.

Unlike traditional supercapacitors where the performance is evaluated per weight of the active material, the footprint area of MSCs becomes the key consideration, making the spacial energy and power density the most important performance metrics.^[35] Figure 5 and Figure S27 (Supporting Information) show the Ragone plots demonstrating the areal and volumetric energy and power density of LIG-related MSCs and their comparison with commercially available energy storage devices. In the LIG-MnO₂-MSCs, the highest energy densities are 32.4 $\mu\text{Wh cm}^{-2}$ and 3.2 mWh cm⁻³, which is an increase of >1200 and >290 times, respectively, compared with LIG at a current density of 0.5 mA cm⁻² (Table S1, Supporting Information). For LIG-PANI-MSCs, the highest energy densities are 8.0 $\mu\text{Wh cm}^{-2}$ and 1.1 mWh cm⁻³, which are 41 and

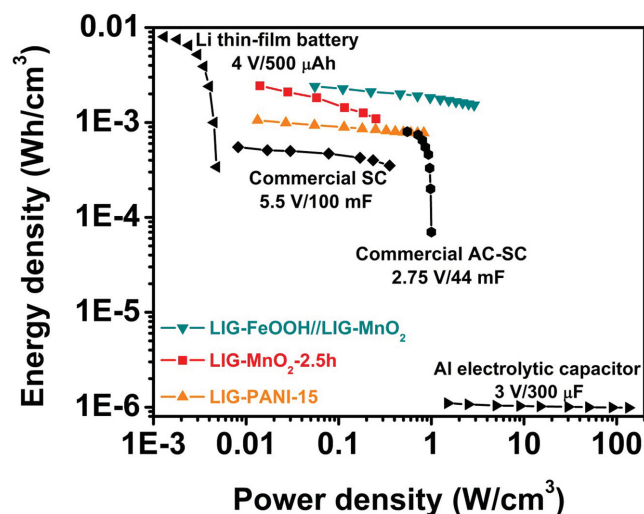


Figure 5. Ragone plots of LIG-MnO₂-2.5 h, LIG-PANI-15, and LIG-FeOOH//LIG-MnO₂. Volumetric energy and power density of LIG-MnO₂-2.5 h, LIG-PANI-15, and LIG-FeOOH//LIG-MnO₂, and their comparison with commercially available energy storage devices. The data for the Li thin-film battery, Al electrolytic capacitor, commercial supercapacitor (SC), and activated carbon supercapacitor (AC-SC) are reproduced from refs.[8,23,24,38].

15 times higher, respectively, than that of LIG at a current density of 0.5 mA cm⁻² (Table S1, Supporting Information). For LIG-FeOOH//LIG-MnO₂, they are 9.6 μWh cm⁻² and 2.4 mWh cm⁻³, respectively. Such energy densities from LIG-MnO₂, LIG-PANI, and LIG-FeOOH//LIG-MnO₂ are much higher than some typical commercial supercapacitors (SCs) (2.75 V/44 mF and 5.5 V/100 mF), and even comparable to Li thin-film batteries (4 V/500 μAh).^[16,36] The maximum areal and volumetric power densities are 2334 μW cm⁻² and 298 mW cm⁻³ for LIG-MnO₂, 649 μW cm⁻² and 1511 mW cm⁻³ for LIG-PANI, and 11853 μW cm⁻² and 2891 mW cm⁻³ for FeOOH//LIG-MnO₂, are comparable to commercial SCs, and >100 times higher than in Li thin-film batteries. The performance of these MSCs show much better performance than our previously studied LIG-MSCs and boron doped LIG-MSCs in aqueous or polymeric acidic electrolyte (Figure S28, Supporting Information),^[28–30] and also better performance than most other reported carbon and pseudocapacitive materials as shown in Table S2 (Supporting Information).^[8,9,15,17,23,37–43] In most of the results in Table S2 (Supporting Information), high-cost lithography for electrode patterning and often high temperature and multistep synthetic processes are required. In this work, the synthesis and patterning of LIG are simultaneously achieved in the first step, and both the laser induction step and subsequent electrodepositions are done under mild temperature and ambient atmosphere.

We have demonstrated a simple route to make all-solid-state flexible MSCs with interdigitated electrodes using a hybrid composite of LIG. The room temperature and ambient air-based laser induction is followed by MnO₂, FeOOH, or PANI electrodeposition. The solid-state flexible symmetric MSCs of LIG-MnO₂ and LIG-PANI, and asymmetric MSCs of LIG-FeOOH//LIG-MnO₂, demonstrate high specific capacitances,

promising energy and power densities, and good cycling stabilities and mechanical flexibilities. These findings not only simplify device fabrication processes with easy control of the size of devices and scalability but also demonstrate the applicability of the LIG technique to a wide range of other pseudocapacitive materials, beyond that of MnO₂, FeOOH, and PANI. Therefore, the design strategy developed here opens up a new avenue for very simply constructing high performance, all-solid-state flexible MSCs.

Experimental Section

Synthesis and Fabrication of LIG: The synthesis and patterning of LIG from a polyimide sheet was done as we described previously.^[29,30] Kapton polyimide films (McMaster-Carr, Cat. No. 2271K3, thickness: 0.005") were used as received. LIG was generated using a CO₂ laser cutter system (Universal X-660 laser cutter platform) on Kapton polyimide film at a power of 4.8 W. All samples were prepared under room temperature and ambient air. LIG was patterned into 12 interdigitated electrodes with a length of 4.1 mm, a width of 1 mm, and a spacing of ≈300 μm between two neighboring microelectrodes (Figure S13, Supporting Information). After that, Pellico colloidal silver paint (No. 16034, Ted Pella) was first applied on the common areas of both electrodes for better electrical contact. The electrodes were then extended with conductive copper tape which were connected to an electrochemical workstation for testing. A Kapton polyimide tape was employed followed by an epoxy (Machineable-fast set, Reorder # 04002, Hardman) sealing to protect the common areas of the electrodes from electrolyte.

Synthesis of LIG-MnO₂: Electrodeposition of MnO₂ on LIG was achieved with a three-electrode setup. LIG on a PI sheet served as the working electrode, which was immersed into an aqueous solution containing 0.01 M Mn(CH₃COO)₂ at ≈60 °C. Platinum foil (Sigma-Aldrich) was the counter electrode and Ag/AgCl (Fisher Scientific) was the reference electrode. A constant current density of 1 mA cm⁻² was applied for a designated time to ensure good deposition of MnO₂ on the sample. The amount of MnO₂ onto LIG was controlled by adjusting the deposition time. After electrodeposition, the sample was withdrawn and washed with deionized (DI) water to remove excess electrolyte and then placed in a vacuum desiccator overnight (≈120 mm Hg).

Synthesis of LIG-FeOOH: Electrodeposition of FeOOH on LIG was achieved with a two-electrode setup. LIG on a PI sheet served as the working electrode, which was immersed into an aqueous solution containing 0.1 M FeCl₃. The pH of FeCl₃ solution was 2, adjusted by 1.0 M HCl. Ag/AgCl (Fisher Scientific) worked as the reference electrode and counter electrode. A constant current density of 15 mA cm⁻² was applied for a designated time to ensure sufficient deposition of FeOOH on the sample. The amount of FeOOH onto LIG was controlled by adjusting the deposition time. After electrodeposition, the sample was withdrawn and washed with DI water to remove excess electrolyte and then placed in a vacuum desiccator overnight (≈120 mm Hg).

Synthesis of LIG-PANI: Electrodeposition of PANI on LIG was achieved with a three-electrode setup. LIG on a PI sheet served as the working electrode, which was immersed into an aqueous solution containing 0.1 M aniline and 1.0 M H₂SO₄. With a platinum counter electrode and Hg/HgCl₂ (Fisher Scientific) reference electrode, PANI was electrochemically deposited onto LIG by cycling within the potential window from -0.20 to 0.95 V versus Hg/HgCl₂. The amount of PANI onto LIG was controlled by the cycle number of deposition. After electrodeposition, LIG-PANI was treated with 1.0 M H₂SO₄ for 1 h. A uniform dark green film was obtained after washing with DI water to remove excess electrolyte and drying in a vacuum desiccator overnight (≈120 mm Hg).

Fabrication of the Flexible All-Solid-State MSCs: Polymeric gel electrolytes of PVA/LiCl and PVA/H₂SO₄ were prepared according to the previously reported method^[16,44] and used in LIG-MnO₂ and

LIG-FeOOH//LIG-MnO₂, and LIG-PANI, respectively. For PVA/LiCl, it was made by stirring 10 mL of DI water, 2.0 g of LiCl (Sigma-Aldrich), and 1.0 g of PVA ($M_w = 50\,000\text{ g mol}^{-1}$, Aldrich No. 34158-4) at 80 °C overnight. For PVA/H₂SO₄, it was made by stirring 10 mL of DI water, 1.0 mL of sulfuric acid (98%, Sigma-Aldrich), and 1.0 g of PVA at 80 °C overnight. ≈0.25 mL of the electrolyte was applied to the active area of the devices, and was dried under ambient conditions for 4 h. The all-solid-state MSCs were obtained after drying in a vacuum desiccator (≈120 mm Hg) overnight for further solidification of the electrolyte.

Electrochemical Characterization of the Flexible All-Solid-State MSCs: The electrochemical performances of the flexible all-solid-state MSCs were characterized by CV and galvanostatic charge–discharge experiments using an electrochemical station (CHI 660D). The areal specific capacitance (C_A) and volumetric specific capacitance (C_V) of electrode materials were calculated from galvanostatic charge–discharge curves according to Equations (1) and (2), respectively:

$$C_A = 4I / (A_{\text{Device}} \times (dV / dt)) \quad (1)$$

$$C_V = 4I / (V_{\text{Device}} \times (dV / dt)) \quad (2)$$

where I is the current applied, A_{Device} is the total area of the device (Figure S13, Supporting Information), V_{Device} is the total volume of the device (Figure S13, Supporting Information), and dV/dt is the slope of the discharge curve.

The areal capacitance ($C_{\text{Device,A}}$) and volumetric capacitance ($C_{\text{Device,V}}$) of the MSCs were calculated by using Equations (3) and (4), respectively:

$$C_{\text{Device,A}} = C_A / 4 \quad (3)$$

$$C_{\text{Device,V}} = C_V / 4 \quad (4)$$

The areal energy density ($E_{\text{Device,A}}$) and volumetric energy density ($E_{\text{Device,V}}$) of the MSCs were calculated by using Equations (5) and (6), respectively:

$$E_{\text{Device,A}} = C_{\text{Device,A}} V^2 / (2 \times 3600) \quad (5)$$

$$E_{\text{Device,V}} = C_{\text{Device,V}} V^2 / (2 \times 3600) \quad (6)$$

where V is the applied voltage.

The areal power density ($P_{\text{Device,A}}$) and volumetric power density ($P_{\text{Device,V}}$) of the MSCs were calculated by using Equations (7) and (8), respectively:

$$P_{\text{Device,A}} = E_{\text{Device,A}} \times 3600 / t \quad (7)$$

$$P_{\text{Device,V}} = E_{\text{Device,V}} \times 3600 / t \quad (8)$$

where t is the discharge time.

Supporting Information

Supporting Information is available from the Wiley Online Library or from the author.

Acknowledgements

L.L., J.Z., and Z.P. contributed equally to this work. This study was funded by the Air Force Office of Scientific Research (AFOSR) Multidisciplinary

University Research Initiative Program (FA9550-12-1-0035), the AFOSR (FA9550-14-1-0111), and the Chinese Scholarship Council.

Received: July 10, 2015

Revised: October 16, 2015

Published online:

- [1] M. Beidaghi, Y. Gogotsi, *Energy Environ. Sci.* **2014**, 7, 867.
- [2] Z. L. Wang, *Nano Today* **2010**, 5, 512.
- [3] J. Bae, M. K. Song, Y. J. Park, J. M. Kim, M. Liu, Z. L. Wang, *Angew. Chem. Int. Ed.* **2011**, 50, 1683.
- [4] D. Yu, K. Goh, H. Wang, L. Wei, W. Jiang, Q. Zhang, L. Dai, Y. Chen, *Nat. Nanotechnol.* **2014**, 9, 555.
- [5] J. Chmiola, C. Largeot, P.-L. Taberna, P. Simon, Y. Gogotsi, *Science* **2010**, 328, 480.
- [6] Z.-S. Wu, X. Feng, H.-M. Cheng, *Natl. Sci. Rev.* **2013**, 1, 277.
- [7] P. Simon, Y. Gogotsi, *Nat. Mater.* **2008**, 7, 845.
- [8] D. Pech, M. Brunet, H. Durou, P. Huang, V. Mochalin, Y. Gogotsi, P.-L. Taberna, P. Simon, *Nat. Nanotechnol.* **2010**, 5, 651.
- [9] J. Lin, C. Zhang, Z. Yan, Y. Zhu, Z. Peng, R. H. Hauge, D. Natelson, J. M. Tour, *Nano Lett.* **2012**, 13, 72.
- [10] C.-C. Liu, D.-S. Tsai, W.-H. Chung, K.-W. Li, K.-Y. Lee, Y.-S. Huang, *J. Power Sources* **2011**, 196, 5761.
- [11] M. Heon, S. Lofland, J. Applegate, R. Nolte, E. Cortes, J. D. Hettinger, P.-L. Taberna, P. Simon, P. Huang, M. Brunet, *Energy Environ. Sci.* **2010**, 4, 135.
- [12] S. Y. Hong, J. Yoon, S. W. Jin, Y. Lim, S.-J. Lee, G. Zi, J. S. Ha, *ACS Nano* **2014**, 8, 8844.
- [13] M. Beidaghi, C. Wang, *Adv. Funct. Mater.* **2012**, 22, 4501.
- [14] M. S. Kim, B. Hsia, C. Carraro, R. Maboudian, *Carbon* **2014**, 74, 163.
- [15] M. F. El-Kady, V. Strong, S. Dubin, R. B. Kaner, *Science* **2012**, 335, 1326.
- [16] M. F. El-Kady, R. B. Kaner, *Nat. Commun.* **2013**, 4, 1475.
- [17] W. Gao, N. Singh, L. Song, Z. Liu, A. L. M. Reddy, L. Ci, R. Vajtai, Q. Zhang, B. Wei, P. M. Ajayan, *Nat. Nanotechnol.* **2011**, 6, 496.
- [18] D. C. Marcano, D. V. Kosynkin, J. M. Berlin, A. Sinitskii, Z. Sun, A. Slesarev, L. B. Alemany, W. Lu, J. M. Tour, *ACS Nano* **2010**, 4, 4806.
- [19] A. M. Dimiev, L. B. Alemany, J. M. Tour, *ACS Nano* **2012**, 7, 576.
- [20] P. Simon, Y. Gogotsi, *Acc. Chem. Res.* **2013**, 46, 1094.
- [21] M. Xue, Z. Xie, L. Zhang, X. Ma, X. Wu, Y. Guo, W. Song, Z. Li, T. Cao, *Nanoscale* **2011**, 3, 2703.
- [22] C.-H. Chen, D.-S. Tsai, W.-H. Chung, K.-Y. Lee, Y.-M. Chen, Y.-S. Huang, *J. Power Sources* **2012**, 205, 510.
- [23] X. Wang, B. D. Myers, J. Yan, G. Shekawat, V. Dravid, P. S. Lee, *Nanoscale* **2013**, 5, 4119.
- [24] M. Xue, F. Li, J. Zhu, H. Song, M. Zhang, T. Cao, *Adv. Funct. Mater.* **2012**, 22, 1284.
- [25] K. Wang, W. Zou, B. Quan, A. Yu, H. Wu, P. Jiang, Z. Wei, *Adv. Energy Mater.* **2011**, 1, 1068.
- [26] G. Wang, L. Zhang, J. Zhang, *Chem. Soc. Rev.* **2012**, 41, 797.
- [27] F. Wang, S. Xiao, Y. Hou, C. Hu, L. Liu, Y. Wu, *RSC Adv.* **2013**, 3, 13059.
- [28] Z. Peng, R. Ye, J. A. Mann, D. Zakhidov, Y. Li, P. R. Smalley, J. Lin, J. M. Tour, *ACS Nano* **2015**, 9, 5868.
- [29] Z. Peng, J. Lin, R. Ye, E. L. Samuel, J. M. Tour, *ACS Appl. Mater. Interfaces* **2015**, 7, 3414.
- [30] J. Lin, Z. Peng, Y. Liu, F. Ruiz-Zepeda, R. Ye, E. L. Samuel, M. J. Yacaman, B. I. Yakobson, J. M. Tour, *Nat. Commun.* **2014**, 5, 5714.
- [31] G. M. Do Nascimento, M. Temperini, *J. Raman Spectrosc.* **2008**, 39, 772.

- [32] L. Li, A.-R. O. Raji, H. Fei, Y. Yang, E. L. Samuel, J. M. Tour, *ACS Appl. Mater. Interfaces* **2013**, 5, 6622.
- [33] L. Li, A. R. O. Raji, J. M. Tour, *Adv. Mater.* **2013**, 25, 6298.
- [34] B. E. Conway, *Scientific Fundamentals and Technological Applications*, Kluwer Academic, New York **1999**.
- [35] Y. Gogotsi, P. Simon, *Sci. Mag.* **2011**, 334, 917.
- [36] W. Zuo, C. Wang, Y. Li, J. Liu, *Sci. Rep.* **2015**, 5, 7780.
- [37] D. Pech, M. Brunet, P.-L. Taberna, P. Simon, N. Fabre, F. Mesnilgrente, V. Conédéra, H. Durou, *J. Power Sources* **2010**, 195, 1266.
- [38] W. W. Liu, Y. Q. Feng, X. B. Yan, J. T. Chen, Q. J. Xue, *Adv. Funct. Mater.* **2013**, 23, 4111.
- [39] J. Feng, X. Sun, C. Wu, L. Peng, C. Lin, S. Hu, J. Yang, Y. Xie, *J. Am. Chem. Soc.* **2011**, 133, 17832.
- [40] M. Beidaghi, W. Chen, C. Wang, *J. Power Sources* **2011**, 196, 2403.
- [41] M. Beidaghi, C. Wang, *Electrochim. Acta* **2011**, 56, 9508.
- [42] E. Eustache, R. Frappier, R. L. Porto, S. Bouhtiyia, J.-F. Pierson, T. Brousse, *Electrochem. Commun.* **2013**, 28, 104.
- [43] Z. S. Wu, K. Parvez, X. Feng, K. Müllen, *Nat. Commun.* **2013**, 4, 2487.
- [44] G. Wang, X. Lu, Y. Ling, T. Zhai, H. Wang, Y. Tong, Y. Li, *ACS Nano* **2012**, 6, 10296.